Theory of phase spectroscopy in bimodal atomic force microscopy

— Source link ↗

Jose R. Lozano, Ricardo Garcia

Institutions: Spanish National Research Council

Related papers:

- Compositional mapping of surfaces in atomic force microscopy by excitation of the second normal mode of the microcantilever

- Theory of multifrequency atomic force microscopy.

- The emergence of multifrequency force microscopy

- Dynamic atomic force microscopy methods

- Systematic achievement of improved atomic-scale contrast via bimodal dynamic force microscopy

Theory of phase spectroscopy in bimodal atomic force microscopy

Jose R. Lozano and Ricardo Garcia[*]

Instituto de Microelectrónica de Madrid, CSIC, Isaac Newton 8, 28760 Tres Cantos, Madrid, Spain
(Received 31 July 2008; revised manuscript received 11 November 2008; published 20 January 2009)

We develop a theoretical formalism to describe bimodal atomic force microscopy (AFM) experiments. The theory relates observables such as amplitudes and phase shifts to physical properties of the tip-surface interaction. The theory is compatible with point-mass and continuous models of the cantilever-tip system. We explain the ability of the bimodal AFM to map compositional variations under the influence of very small conservative forces. This is achieved by representing the dependence of the phase shift or amplitude of one eigenmode with respect to the amplitude or phase shift of the other mode. The agreement obtained between the theory and the numerical simulations validates the theoretical formalism.

I. INTRODUCTION

The atomic force microscope (AFM) is a versatile tool for analyzing and characterizing a variety of systems and structures at the nanoscale,[1–9] as well as for developing nanoscale devices.[10–12] In the amplitude modulation (AM) mode[13] (AM-AFM), either the sample or the tip is scanned in a raster fashion while a feedback mechanism keeps the oscillation amplitude of the cantilever-tip system a fixed value (set-point amplitude). The variations in the z-scanner position are reported as topographic images while the variations in the phase shift between the external excitation and the cantilever response provide a compositional map of the surface. The feedback controls the motion of the z scanner which, in turns, sets the distance between the cantilever base and the sample.

Amplitude modulation AFM was initially designed to excite the cantilever near or at its fundamental free resonance frequency. However, the need to improve compositional contrast and to provide quantitative information about material properties have stimulated the development of methods based on the detection and/or excitation of higher harmonics[14–17] or modes.[18–26] In particular, multifrequency excitation schemes[27–30] have opened different channels to extract information about material properties. In bimodal AFM operation, the cantilever is simultaneously excited by two different driving forces. The excitation frequencies are tuned to match two of the flexural modes of the cantilever, usually the first and second flexural resonances, although it could be applied to any other pair of frequencies,[31] and even over a band of frequencies.[32]

It has been shown that bimodal AFM could result in higher force sensitivity and compositional contrast while imaging organic conjugated materials[33] or isolated proteins in air[29] and liquids.[30] In bimodal AFM, the amplitude of the first mode is used to track the topography while some parameters of the second mode, either the amplitude or the phase shift or both, are used as complementary channels to explore the tip-surface forces and, more importantly, to increase the force sensitivity or compositional contrast to detect mechanical or electrical[34] interactions. Proksch[33] showed maps of a graphite surface that can be related to its electronic properties. Bostanci et al.[35] used the first flexural mode of the can-

tilever to stabilize the tip-sample separation while the second mode signal monitored the presence of charges on a substrate. San Paulo et al.[36] utilized the extra sensitivity of multifrequency excitation to measure subnanometer mechanical vibrations in resonant devices. Maximum tip-molecule forces of 35 pN have been reported while imaging antibodies.[29] Rodriguez et al.[37] used the bimodal excitation method to develop a resonant-frequency tracking scanning probe microscope based on amplitude detection. Bimodal AFM excitation can also be used to suppress the bistable motion of the cantilever.[38] Recently, Martinez et al.[30] reported high-resolution images of antibodies in liquids. Bimodal AFM has successfully been combined with nanotomography to image polymer materials.[39]

In a previous contribution we have identified the origin of the high force sensitivity observed in bimodal AFM imaging in the absence of dissipative interactions.[40] An analytical model based on the energy conservation principle and the virial theorem was proposed to relate phase shifts and amplitudes to material properties. In Sec. II we explicitly deduce the relationships between the experimental parameters and the virial of the tip-surface forces for a point-mass system. We extend the theory to include both dissipative and conservative forces. In Sec. III we generalize the theory to describe continuous oscillators with several flexural resonances. The Euler-Bernoulli equation is decomposed in a set of coupled differential equations. In Sec. IV the model is applied to describe bimodal AFM. We specifically discuss the implications for a linear tip-surface force. In Sec. V we analyze the equivalence between point-mass and continuous models. Section VI provides a summary of the results.

II. POINT-MASS MODEL DESCRIPTION OF THE CANTILEVER-TIP SYSTEM

As a first approximation, we consider the cantilever-tip ensemble as a point-mass object. Its instantaneous deflection $z(t)$ is described by the second Newton's law differential equation[41] (see Fig. 1)

$$m\ddot{z}(t) = -kz(t) - \frac{m\omega_0}{Q}\dot{z}(t) + F_{t\text{-}s}(d) + F_0 \cos \omega t, \quad (1)$$

where m is the cantilever-tip effective mass, k parametrizes the elastic response of the cantilever, while the quality factor
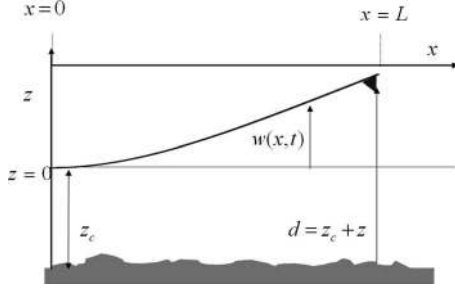
FIG. 1. Schematics of the cantilever-tip system. z is the instantaneous tip deflection, z_c is the average position, d is the instantaneous tip-surface distance, x is the spatial coordinate along the longitudinal cantilever axis, and $w(x,t)$ is the instantaneous cantilever bending.

Q parametrizes the hydrodynamic damping. The free resonance frequency of the system is

$$\omega_0 = \sqrt{k/m} \quad (2)$$

and F_0 and ω are, respectively, the amplitude and frequency of excitation force (in what follows $\omega = \omega_0$). $F_{t\text{-}s}(d)$ represents the interaction between tip and sample. The instantaneous tip-surface distance is represented by

$$d = z_c + z(t) \quad (3)$$

with z_c as the average tip-surface distance. By neglecting the average cantilever deflection and the higher harmonics of the oscillation, we approximate the instantaneous tip deflection by

$$z(t) = A \cos(\omega_0 t - \phi). \quad (4)$$

By applying the energy conservation principle and the virial theorem[42] over one period of the oscillation $T_0 \equiv 2\pi/\omega_0$, we derive analytical relationships between the observables and the tip-surface force parameters. Those equations link amplitudes and phase shifts to two independent properties of the tip-surface interaction, the dissipated energy and the virial, which are determined by

$$E_{t\text{-}s} \equiv -\int_0^{T_0} dt\, F_{t\text{-}s}(d)\dot{z}(t) = \frac{\pi k A}{Q}(A_0 \sin\phi - A), \quad (5)$$

$$V_{t\text{-}s} \equiv \frac{1}{T}\int_0^{T_0} dt\, F_{t\text{-}s}(d) z(t) = -\frac{kA_0}{2Q} A \cos\phi \quad (6)$$

with $A_0 = F_0 Q/k$ as the free amplitude value.

Equation (5) represents the convolution of the interaction with the velocity and Eq. (6) the convolution of the interaction with the position. We remark that both expressions are mathematically independent. The validity of the above equations is confirmed by numerical simulations (Fig. 2). A tip-surface interaction described by

$$F_{t\text{-}s}(d) = \frac{1}{d^2}\left[\alpha_c + \alpha_{nc}\frac{\dot{z}(t)}{|\dot{z}(t)|}\right] \quad (7)$$

has been used in order to introduce long-range dissipative and conservatives forces. The first term describes the conser-
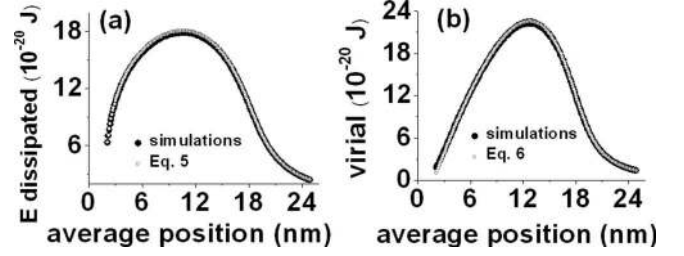

FIG. 2. Comparison between simulations and theory as given by Eqs. (5) and (6). (a) Virial of the interaction. (b) Energy dissipated by the tip-sample forces. Filled symbols correspond to the numerical simulations while open circles stand for the theory.

vative part of the force as given by the van der Waals expression between a flat surface and a sphere. Its strength is controlled by the interfacial constant α_c. The second term gives the dissipative part of the force. It is composed by the same distance dependence as the conservative part, but this time dissipation is included by adding a factor that depends on the sign of the velocity. It can be shown that this is equivalent to considering a van der Waals tip-surface interaction with a different Hamaker constant value when approaching and retracting.[43]

The numerical solution of Eq. (1) was calculated by using a fourth-order Runge-Kutta algorithm.[44] The values used for the resonance frequency, spring constant, and quality factor of the cantilever are $f_0 = 49$ kHz, $k = 0.9$ N/m, and $Q = 255$, respectively. The tip-sample interaction was characterized by $\alpha_c = 3.01 \times 10^{-28}$ J m and $\alpha_{nc} = 0.43\alpha_c = 1.29 \times 10^{-28}$ J m. The value of the free amplitude was $A_0 = 17$ nm and the tip radius was $R = 20$ nm. We have verified that for the above parameters the tip never touches the sample; consequently, Eq. (7) does not diverge.

To express the observables as a function of the tip-surface forces, we define two nondimensional quantities proportional to the dissipated energy and the virial of the force, respectively, as follows:

$$\beta \equiv \frac{QE_{t\text{-}s}}{kA_0^2}, \quad (8)$$

$$v \equiv \frac{QV_{t\text{-}s}}{kA_0^2}. \quad (9)$$

By using the following change in variables:

$$x \equiv \frac{A\cos\phi}{A_0}, \quad (10)$$

$$y \equiv \frac{A\sin\phi}{A_0}, \quad (11)$$

Eqs. (5) and (6) can be expressed as
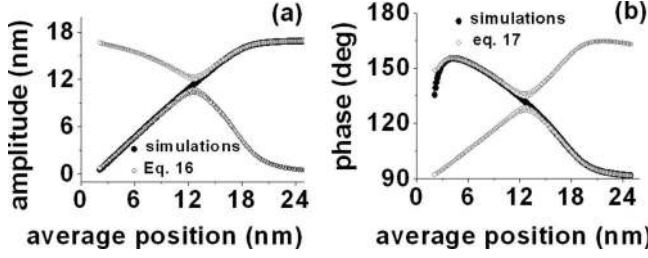
$$v = -\frac{1}{2}x, \quad (12)$$

FIG. 3. Comparison between simulations and theory. The experimental observables, (a) amplitude and (b) phase shift of the cantilever response, are plotted together with their respective reconstructions given from virial and energy dissipation values [Eqs. (16) and (17), respectively].

$$\beta = \pi(y - x^2 - y^2). \tag{13}$$

By inverting Eqs. (12) and (13) we get

$$x = -2v \tag{14}$$

$$y = \frac{1 \pm \sqrt{1 - (4v)^2 - 4\beta/\pi}}{2} \tag{15}$$

Finally, we deduce the expressions for the amplitude and the phase shift as function of the tip-surface force properties,

$$A = A_0\sqrt{x^2 + y^2} = A_0\sqrt{(2v)^2 + \left(\frac{1 \pm \sqrt{1 - (4v)^2 - 4\beta/\pi}}{2}\right)^2}, \tag{16}$$

$$\phi = \text{arctg}\left(\frac{y}{x}\right) = -\text{arctg}\left(\frac{1 \pm \sqrt{1 - (4v)^2 - 4\beta/\pi}}{4v}\right). \tag{17}$$

Figures 3(a) and 3(b) show the reconstruction of the amplitude and phase shift, respectively, as given by Eqs. (16) and (17). The values used for v and β were taken from numerical solution of Eq. (1). The numerical values of amplitude and phase provided by simulations are also plotted. We found a satisfactory agreement between the numerical solution and the algebraic approach. The sign $\pm$ in Eqs. (16) and (17) gives rise to two branches in the reconstruction of amplitude and phase-shift curves. The guideline to select the proper curves is given by the fact that the amplitude decreases with the average tip-surface distance.

III. CONTINUOUS MODEL OF THE CANTILEVER-TIP SYSTEM

The point-mass model cannot describe the influence of higher eigenmodes on the tip motion. The continuous character of the cantilever is captured by solving the Euler-Bernoulli equation. This equation describes the bending of a rectangular and homogeneous cantilever along its longitudinal axis.

The Euler-Bernoulli equation for a continuous and uniform cantilever beam under the action of external forces applied at its free end is

$$EI\frac{\partial}{\partial x^4}\left[w(x,t) + a_1\frac{\partial w(x,t)}{\partial t}\right] + \rho bh\frac{\partial^2 w(x,t)}{\partial t^2}$$

$$= -a_0\frac{\partial w(x,t)}{\partial t} + \delta(x - L)[F_{\text{exc}}(t) + F_{t\text{-}s}(d)]. \tag{18}$$

E is the cantilever's Young's modulus; I is the area moment of inertia; a_1 is the internal damping coefficient; ρ is the mass density; b, h, and L are, respectively, the width, height, and length of the cantilever; a_0 is the hydrodynamic damping; $w(x,t)$ is the time-dependent vertical displacement of the differential beam's element placed at the x position (Fig. 1); $F_{\text{exc}}(t)$ is the excitation force; while the tip-surface interaction is represented by $F_{t\text{-}s}(d)$ with

$$d = z_c + w(L,t) \tag{19}$$

as the instantaneous tip-surface separation.

We substitute the ansatz $w(x,t) = \varphi(x)Y(t)$ in Eq. (18) and apply the following boundary conditions:

$$\varphi(0) = 0 \quad \text{(vertical displacement at } x = 0 \text{ is zero),}$$
$$\tag{20a}$$

$$\varphi'(0) = 0 \quad \text{(slope at } x = 0 \text{ is zero),} \tag{20b}$$

$$\varphi''(L) = 0 \quad \text{(vertical internal torque at } x = L \text{ is zero),}$$
$$\tag{20c}$$

$$\varphi'''(L) = 0 \quad \text{(vertical internal force at } x = L \text{ is zero).}$$
$$\tag{20d}$$

The cantilever at $x = 0$ is clamped [Eqs. (20a) and (20b)] while it is free at $x = L$ [Eqs. (20c) and (20d)]. The above boundary conditions introduce a discrete number of solutions to Eq. (18), then the vertical displacement can be expanded into a series of eigenmodes,

$$w(x,t) = \sum_{n=1}^{\infty} \varphi_n(x)Y_n(t), \tag{21}$$

where $\varphi_n(x)$ can be defined as[45]

$$\varphi_n(x) = \cos\left(\kappa_n\frac{x}{L}\right) - \cosh\left(\kappa_n\frac{x}{L}\right)$$
$$- \frac{\cos(\kappa_n) + \cosh(\kappa_n)}{\sin(\kappa_n) + \sinh(\kappa_n)}\left[\sin\left(\kappa_n\frac{x}{L}\right) - \sinh\left(\kappa_n\frac{x}{L}\right)\right] \tag{22}$$

with κ_n as the nth positive real root of the equation

$$1 + \cos\kappa_n\cosh\kappa_n = 0 \tag{23}$$

and

$$\int_o^L dx\,\varphi_n(x)\varphi_m(x) = L\delta_{n,m}, \tag{24}$$

$$\varphi_n(0) = 0, \tag{25}$$

$$\varphi_n(L) = 2(-1)^n. \tag{26}$$

On the other hand, the time-dependent function for each eigenmode, $Y_n(t)$, obeys the set of anharmonic differential equations

$$\ddot{Y}_n(t) + \frac{\omega_n}{Q_n}\dot{Y}_n(t) + \omega_n^2 Y_n(t) = \frac{F_n(t)}{m_n}, \quad n = 1, 2, \ldots \quad (27)$$

where the eigenmode resonances, effective masses, quality factors, and external forces are defined by

$$\omega_n^2 = \left(\frac{\alpha_n}{L}\right)^4 \frac{EI}{\rho b h}, \quad (28)$$

$$m_n = \rho b h \int_0^L dx [\varphi_n(x)]^2 = \rho b h L \equiv m_c, \quad (29)$$

$$Q_n = \frac{\omega_n}{\frac{a_0}{\rho b h} + a_1 \omega_n^2}, \quad (30)$$

$$F_n(t) = \int_0^L dx \, f_{ext}(x,t) \varphi_n(x)$$
$$= \int_0^L dx \, \delta(x - L)[F_{t-s}(d) + F_{exc}(t)]\varphi_n(x)$$
$$= 2(-1)^n [F_{t-s}(d) + F_{exc}(t)]. \quad (31)$$

The total mass of the cantilever is expressed as m_c while $f_{ext}(x,t)$ represents the density of external forces per length. Then, the actual tip motion can be calculated as

$$w(L,t) = \sum_{n=1}^{\infty} \varphi_n(L) Y_n(t) = \sum_{n=1}^{\infty} 2(-1)^n Y_n(t) \equiv \sum_{n=1}^{\infty} z_n(t), \quad (32)$$

where $z_n(t)$ is the modal projection of the tip motion. Combination of the above definitions and Eq. (27) gives the corresponding differential equation for $z_n(t)$,

$$\ddot{z}_n(t) + \frac{\omega_n}{Q_n}\dot{z}_n(t) + \omega_n^2 z_n(t) = \frac{F_{exc}(t) + F_{t-s}(d)}{m}, \quad n = 1, 2, \ldots \quad (33)$$

with

$$m = 0.25 m_c. \quad (34)$$

It is shown then that the modal effective mass m is one fourth of the total mass of the cantilever. This is true whenever we deal with homogeneous and rectangular cantilevers. Each mode is described by its modal parameters, eigenfrequency ω_n, spring constant $k_n = m\omega_n^2$, and quality factor Q_n. We also remark that the effective mass of the point-mass model (Sec. II) coincides with m as defined in Eq. (34) (see Sec. V).

To calculate the numerical solution of the displacement [Eq. (32)] we just consider the contributions from the first four normal modes. The displacement of each mode is obtained by solving Eq. (33) with four coupled fourth-order Runge-Kutta algorithms.[46]

IV. BIMODAL AFM MODEL

Bimodal AFM is characterized by the simultaneous excitation of two cantilever resonances, usually the lowest eigenmodes,

$$F_{exc}(t) = F_1 \cos \omega_1 t + F_2 \cos \omega_2 t, \quad (35)$$

where ω_1 and ω_2 are the first two eigenfrequencies and $F_i \equiv \frac{k_i A_{0i}}{Q_i}$ are the modal excitation force, while A_{0i} are the modal free amplitude values; $i = 1, 2$.

It has already been shown[40] that the instantaneous tip deflection could be approximated by the addition of two component waves, $w = z_1 + z_2$. Each component follows the modal Eq. (33) where n is either 1 or 2. Then, we can apply the virial and energy conservation theorems in the same way that was done for the point-mass system (Sec. II). We can define the modal dissipated energy and virial of the interaction as

$$E_{t-s}(i) \equiv -\int_0^T dt \, F_{t-s}(d)\dot{z}_i(t), \quad (36)$$

$$V_{t-s}(i) \equiv \frac{1}{T}\int_0^T dt \, F_{t-s}(d) z_i(t), \quad (37)$$

and their corresponding reduced magnitudes as

$$\beta_i \equiv \frac{Q_i E_{t-s}(i)}{k_i A_{0i}^2}, \quad (38)$$

$$v_i \equiv \frac{Q_i V_{t-s}(i)}{k_i A_{0i}^2}, \quad (39)$$

where $i = 1, 2$.

In that case we integrate over the period $T \equiv p_1 \frac{2\pi}{\omega_1} = p_2 \frac{2\pi}{\omega_2}$, in which the signal $w(L,t)$ is periodic. For this it is required that the eigenmode frequencies, ω_1 and ω_2, are commensurable; i.e., $\omega_1/\omega_2 = p_1/p_2$ for a certain pair of integers p_1 and p_2 (this is always possible with high accuracy).

A. Tip-surface conservative interactions

In this case, $E_{t-s}(i) = 0$ which implies $\beta_i = 0$, then

$$\phi_i = \text{arctg}\left(\frac{1 \pm \sqrt{1 - (4v_i)^2}}{4v_i}\right). \quad (40)$$

Figure 4 shows the bimodal amplitude and the phase-shift curves. The curves of the first mode are very similar to the ones obtained under monomodal excitation. However, the amplitude and the phase curves of the second mode show the presence of an inflection point at intermediate values of the average tip-surface distance. The existence of an inflection
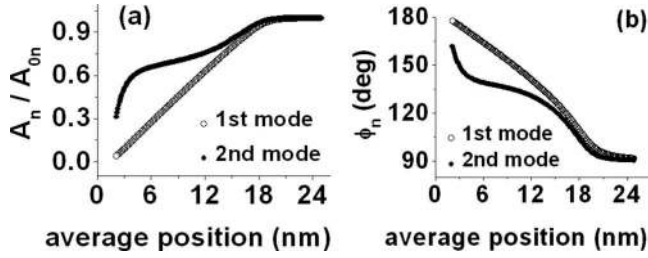
FIG. 4. Dependence of the amplitude and phase shift on the average tip position for bimodal AFM operation (numerical simulations). (a) Normalized first (open dots) and second mode amplitudes (black dots). (b) First (open dots) and second mode (black dots) phase shifts. The tip-surface interaction is modeled by a van der Waals force for a sphere-flat geometry characterized by H $=9.03 \times 10^{-20}$ J and $R=20$ nm.

point is controlled by the amplitude ratio A_{01}/A_{02}. Higher amplitude ratios produce the inflection point.

Generalization of Eqs. (5) and (6) to both modes and no dissipation in the system gives the relationships

$$E_{t-s}(i) = \frac{\pi k_i A_i}{Q_i}(A_{0i} \sin \phi_i - A_i) = 0, \qquad (41)$$

$$V_{t-s}(i) = -\frac{k_i A_{0i}}{2Q_i} A_i \cos \phi_i. \qquad (42)$$

From Eq. (41) we deduce

$$A_i = A_{0i} \sin \phi_i, \qquad (43)$$

where A_i and ϕ_i are, respectively, the amplitude and phase shift of the ith mode. Equation (43) states that, for a given eigenmode, its phase shift is completely determined by the free and the interacting amplitudes of that mode. Consequently, at fixed A_i, changes in material properties would not produce changes in the phase shift.

Material contrast can be achieved by using a representation that combines parameters of both modes. We call this as a cross-mode representation. An equation that links the amplitude of one mode with the phase shift of the other mode can be deduced by considering the total virial of the system

$$V_{t-s} = V_{t-s}(1) + V_{t-s}(2) \qquad (44)$$

where the $V_{t-s}(i)$ were defined in Eq. (42).

By combining Eqs. (43) and (44),

$$V_{t-s} = \frac{1}{2}\left[F_1 A_1 \sqrt{1 - \left(\frac{A_1}{A_{01}}\right)^2} - F_2 A_{02} \sin \phi_2 \cos \phi_2\right]. \qquad (45)$$

Figure 5 shows that material contrast due to conservative interactions is only possible for cross-mode representations. Parallel-mode representation, i.e., the representation of the phase shift of one mode with respect to its amplitude, is not sensitive to changes in the Hamaker constant. The dependence of the bimodal phase shift on the material (Hamaker values) is shown in Fig. 6. The phase shift of the second mode is very sensitive to variations in the strength of the
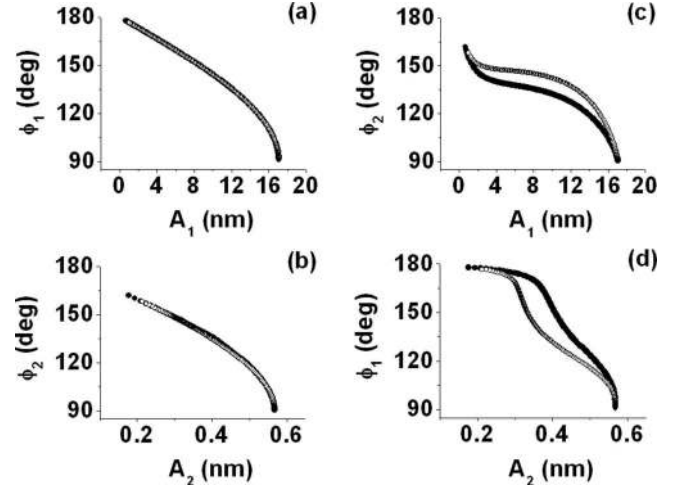

FIG. 5. Bimodal AFM operation and nonlinear forces. Dependence of the phase shift for two different materials (numerical simulations). Parallel-mode representations for (a) first mode and (b) second mode. (c) and (d) Cross-mode representations. The tip-surface interaction is a van der Waals force for a sphere-flat geometry characterized by $R=20$ nm; $H_a=9.03 \times 10^{-20}$ J (dark dots) and $H_b=4.7 \times 10^{-20}$ J (open dots).

attractive force. A 33% change in the Hamaker constant (from 9×10^{-20} to 12×10^{-20} J) implies ϕ_2 changes about 4°, i.e., a factor of 20 above the noise level $\sim$0.2° [Fig. 6(b)].

Figure 7 shows the maximum force exerted by the tip on the sample surface for two different free amplitudes. The curves show that under bimodal excitation the maximum force is below 200 pN. The curves also show that for relatively small amplitudes $\sim$5 nm, the exerted forces are very small, $<$50 pN. Imaging at very small forces is one of the major advantages brought by bimodal AFM excitation with respect to tapping mode AFM operation.

The above simulations have been performed by using the following values: $L=225$ μm, $b=40$ μm, $h=1.8$ μm, and the tip radius $R=20$ nm for the cantilever geometry. The Young's modulus is $E=170$ GPa and its mass density is ρ $=2320$ kg/m^3. They give a value for the first two eigenfrequencies of $\omega_1=48.9$ kHz and $\omega_2=306.6$ kHz. The damping coefficients are $a_0=2 \times 10^{-4}$ kg/m s (external damping) and $a_1=2 \times 10^{-10}$ s (internal damping) which give a value for the modal quality factors of $Q_1=255$ and $Q_2=1000$. The ex-
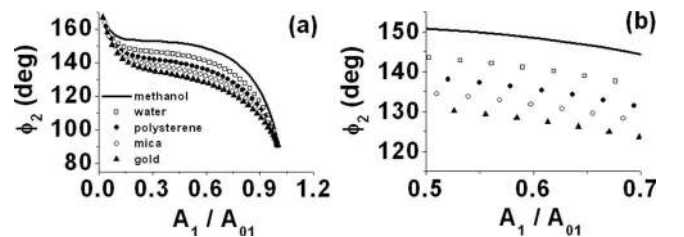

FIG. 6. Phase-shift spectroscopy. Bimodal phase-shift dependence on set-point amplitude ratio for different materials. (a) Second mode phase-shift dependence on A_1/A_{01} for the whole amplitude-ratio range. (b) Second mode phase-shift dependence on A_1/A_{01} for ratios in the 0.5–0.7 range.
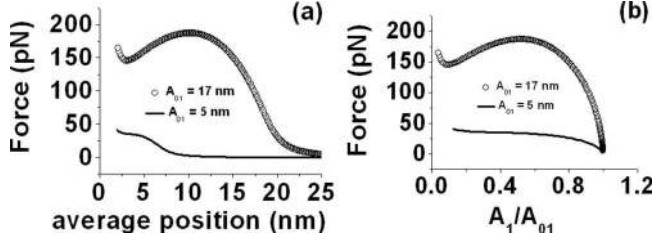
FIG. 7. Calculated maximum force per cycle for two different amplitudes. The continuous line is obtained for $A_{01}=5$ nm, $A_{02}=0.56$ nm, and $R=5$ nm. The dots are obtained for $A_{01}=17$ nm, $A_{02}=0.56$ nm, and $R=20$ nm. The amplitude and phase-shift curves for $A_{01}=17$ nm are shown in Fig. 5. In all the cases the Hamaker constant is $H=9.03\times10^{-20}$ J.

citation forces are $F_1=60$ pN and $F_2=20$ pN that correspond to the free amplitude values $A_{01}=17$ nm and $A_{02}=0.56$ nm. The tip-surface interaction was given by the long-range attractive van der Waals force

$$F_{t\text{-}s}(d) = -\frac{HR}{6d^2} \tag{46}$$

with H being the Hamaker constant. The Hamaker values for an interface composed by a SiO_2-tip and, respectively, gold, mica, polystyrene, water, and methanol surfaces are 12×10^{-20}, 9×10^{-20}, 7×10^{-20}, 5×10^{-20}, and 3×10^{-20} J.

B. Tip-surface conservative linear interactions

It is formative to analyze the operation of the bimodal AFM under a conservative and linear interaction between the tip and the sample surface,

$$F_{t\text{-}s}(z_1,z_2) = \gamma(z_1 + z_2). \tag{47}$$

This system can be exactly solved by applying Eqs. (42) and (43), where the value of the virials for each mode can now be analytically integrated,

$$V_{t\text{-}s}(i) = -\frac{k_i A_{0i}}{2Q_i}A_i \cos\phi_i = \frac{\gamma A_i^2}{2}, \quad i=1,2. \tag{48}$$

By combining Eqs. (43) and (48) we obtain

$$\tan\phi_i = -\frac{k_i}{Q_i\gamma}, \tag{49}$$

$$A_i = \frac{A_{0i}}{\sqrt{1+(Q_i\gamma/k_i)^2}}. \tag{50}$$

We note that γ parametrizes the strength of the interaction, so it contains the average tip-surface distance z_c.

By combining Eqs. (49) and (50) we obtain an expression for the dependence of the phase shift of one mode with respect to the amplitude of the other,

$$\tan\phi_j = \mp\frac{k_i}{k_j}\frac{Q_j}{Q_i}\sqrt{\left(\frac{A_{0i}}{A_i}\right)^2-1}, \quad i,j=1,2. \tag{51}$$

From Eq. (51) we deduce that for a linear and conservative interaction such as the one given by Eq. (47) the cross-mode
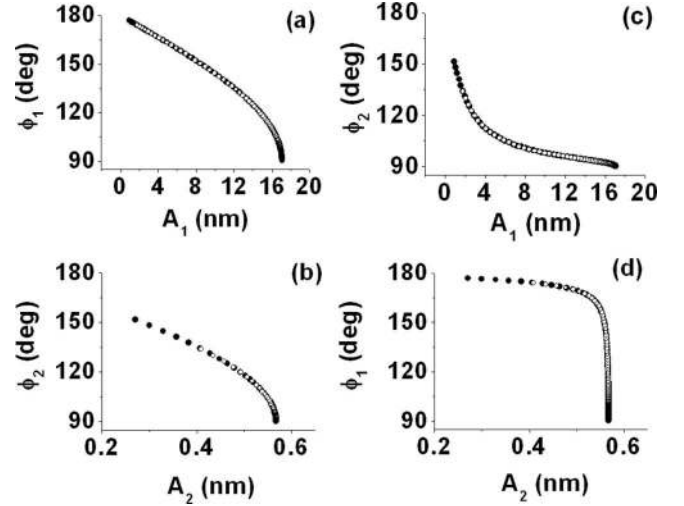

FIG. 8. Bimodal AFM operation and linear forces. Dependence of the phase shift for two different materials (numerical simulations). Parallel-mode representations for (a) first mode and (b) second mode. (c) and (d) Cross-mode representations. The linear tip-surface interaction is characterized by $R=20$ nm; $H_a=9.03\times10^{-20}$ J (dark dots) and $H_b=4.7\times10^{-20}$ J (open dots).

representation does not provide material contrast.

Numerical solution confirms the analytical expressions. Figure 8 shows the dependence of the modal phase shifts ϕ_1 and ϕ_2 with the modal amplitudes A_1 and A_2. A parallel-mode representation [Figs. 8(a) and 8(b)] gives the same arcsine dependence regardless of the material properties and similarly for cross-mode representations [Figs. 8(c) and 8(d)]. At variance with the van der Waals case referred above, the second mode phase shift does not present its characteristic inflection point at intermediate amplitude-ratio values, as was shown in Fig. 5(c). On the contrary, the change in curvature appears for $A_1 \approx A_{01}$, where the cantilever is close to the free state. That atypical behavior is clearly due to the presence of linear interactions.

The same parameters as in Sec. IV A were used for the numerical simulations, with the tip-surface force constant $\gamma = HR/3z_c^3$. That linear force is the first-order term in the Taylor expansion of the van der Waals interaction [Eq. (46)].

C. Tip-surface dissipative interactions

Analytical expressions can also be deduced when the tip-surface force in bimodal AFM has conservative and nonconservative contributions. The procedure to deduce the analytical expressions is identical to the one used in Sec. IV A. Then, the cantilever-tip ensemble will be described by the system of differential modal equations

$$\ddot{z}_n(t) + \frac{\omega_n}{Q_n}\dot{z}_n(t) + \omega_n^2 z_n(t) = \frac{F_1\cos\omega_1 t + F_2\cos\omega_2 t + F_{t\text{-}s}(d)}{m} \tag{52}$$

with $n=1,2$. The solution of the above equation has two components that vibrate with the frequencies ω_n and ω_m with $n\neq m$ and $m=1,2$;

$$z_n(t) = A_n \cos(\omega_n t - \phi_n) + B_m \cos(\omega_m t - \psi_m). \quad (53)$$

Then, we can apply the virial and energy conservation theorems in the same way that was done for the point-mass system (Sec. II). By integrating over the period T, in which the signal $w(L,t)$ is periodic,

$$P_{t\text{-}s}(1) \equiv -\frac{1}{T}\int_0^T dt\, F_{t\text{-}s}(d)\dot{z}_1(t)$$

$$= \frac{1}{2}\left[\frac{\omega_1}{Q_1}k_1 A_1(A_{01}\sin\phi_1 - A_1)\right.$$

$$\left. + k_2 B_1\left(\frac{\omega_2}{Q_2}B_{01}\sin\psi_1 - \frac{\omega_1}{Q_1}B_1\right)\right], \quad (54)$$

$$P_{t\text{-}s}(2) \equiv -\frac{1}{T}\int_0^T dt\, F_{t\text{-}s}(d)\dot{z}_2(t)$$

$$= \frac{1}{2}\left[\frac{\omega_2}{Q_2}k_2 A_2(A_{02}\sin\phi_2 - A_2)\right.$$

$$\left. + k_1 B_2\left(\frac{\omega_1}{Q_1}B_{02}\sin\psi_2 - \frac{\omega_2}{Q_2}B_2\right)\right], \quad (55)$$

$$V_{t\text{-}s}(1) \equiv \frac{1}{T}\int_0^T dt\, F_{t\text{-}s}(d)z_1(t)$$

$$= \frac{1}{2}[-F_1 A_1\cos\phi_1 + (k_1 - k_2)B_1^2 - F_2 B_1\cos\psi_1],$$

$$(56)$$

$$V_{t\text{-}s}(2) \equiv \frac{1}{T}\int_0^T dt\, F_{t\text{-}s}(d)z_2(t)$$

$$= \frac{1}{2}[(k_2 - k_1)B_2^2 - F_2 A_2\cos\phi_2 - F_1 B_2\cos\psi_2].$$

$$(57)$$

We use dissipated power ($P_{t\text{-}s}$) values instead of dissipated energy because the former is a more convenient magnitude when treating signals with different periods. We use the notation B_m and Ψ_m for the amplitude and phase shift at the frequency different from the resonance frequency defined by index n of the left-hand side of Eq. (52). The above expressions can be simplified by neglecting the contribution out of resonance, then

$$P_{t\text{-}s}(1) = \frac{\omega_1 k_1 A_1}{2Q_1}(A_{01}\sin\phi_1 - A_1), \quad (58)$$

$$P_{t\text{-}s}(2) = \frac{\omega_2 k_2 A_2}{2Q_2}(A_{02}\sin\phi_2 - A_2), \quad (59)$$

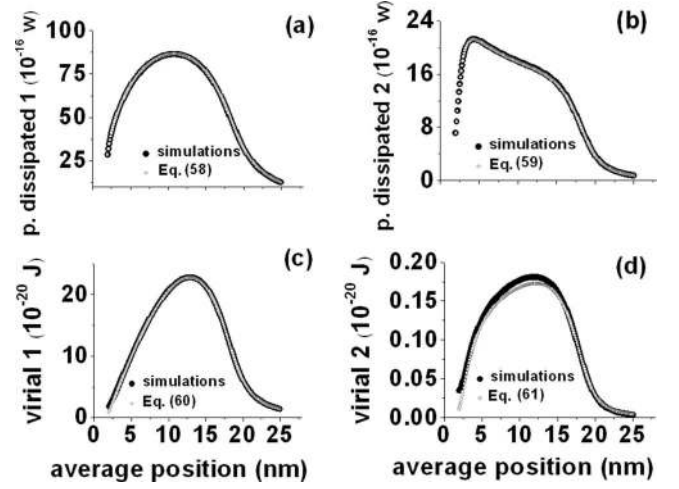$$V_{t\text{-}s}(1) = -\frac{1}{2}F_1 A_1\cos\phi_1, \quad (60)$$

FIG. 9. Bimodal AFM operation. Comparison between theory (open dots) and numerical simulations (dark dots) for the virial and the dissipated power. (a) First mode dissipated power. (b) Second mode dissipated power. (c) First mode virial. (d) Second mode virial. See text for the parameter values used in the numerical solution.

$$V_{t\text{-}s}(2) = -\frac{1}{2}F_2 A_2\cos\phi_2. \quad (61)$$

We can also find the total dissipated power and the total tip-surface interaction virial as

$$V_{t\text{-}s} \equiv \frac{1}{T}\int_0^T dt\, F_{t\text{-}s}(d)w(L,t) = V_{t\text{-}s}(1) + V_{t\text{-}s}(2), \quad (62)$$

$$P_{t\text{-}s} \equiv -\frac{1}{T}\int_0^T dt\, F_{t\text{-}s}(d)\frac{dw(L,t)}{dt} = P_{t\text{-}s}(1) + P_{t\text{-}s}(2).$$

$$(63)$$

Figure 9 shows $P_{t\text{-}s}(n)$ and $V_{t\text{-}s}(n)$ values using Eqs. (58)–(61) compared to numerical solution of Eq. (52) with $n=1,2$. In all cases a good agreement between analytical expressions and simulations is achieved. The calculations have been performed by using the cantilever characteristics and excitation parameters described in Secs. IV A and IV B. For the sample properties, we consider a long-range attractive force with both conservative and dissipative parts, with the same interfacial constant values α_c and α_{nc} as in Sec. II.

V. EQUIVALENCE BETWEEN POINT-MASS AND CONTINUOUS MODELS

Describing the cantilever-tip system by a point-mass model requires the introduction of an effective mass, a quality factor, and a force constant.[22] Here, we derive the relationships among the above effective values and the parameters of the continuous cantilever-tip system. First, we need to identify which mode i dominates the tip dynamics. Then, the tip deflection only carries information on this mode $w(L,t)=z_i(t)$, where we have assumed $x=L$.

We have seen that the total mass of the cantilever is related to the effective mass of a given mode by $m_i = 0.25 m_c$, then

$$k_i = m_i \omega_i^2. \tag{64}$$

Now, we derive the relationship among the different modal force constants and the cantilever's static force constant k_s. The static spring constant is defined as the ratio between a known static force F_0 and the deflection w_0 caused by that force, considering all the modes $(n = 1, 2, \ldots, \infty)$. Then, from Eq. (33) and by taking into account that for a static force z_n does not depend on time, we obtain

$$z_n = \frac{F_0}{k_n} \tag{65}$$

which yields a total deflection

$$w(L, t) = \sum_{n=1}^{\infty} z_n(t) = F_0 \sum_{n=1}^{\infty} \frac{1}{k_n} \equiv \frac{F_0}{k_s}, \tag{66}$$

where the static force constant is defined as

$$k_s = \left(\sum_{n=1}^{\infty} \frac{1}{k_n} \right)^{-1}. \tag{67}$$

For a rectangular and homogeneous cantilever beam it is known[45] that

$$k_n = \frac{\kappa_n^4}{4} \frac{EI}{L^3}. \tag{68}$$

By combining Eqs. (67) and (68) we obtain

$$k_s = \frac{3EI}{L^3}, \tag{69}$$

where we have used[47]

$$\sum_{n=1} \frac{1}{\kappa_n^4} = \frac{1}{12}. \tag{70}$$

In particular, the relationship of the first mode force constant with the cantilever static force constant is

$$\frac{k_1}{k_s} = \frac{\kappa_1^4}{12} = 1.030. \tag{71}$$

We note that the first mode spring constant k_1 coincides with the point-mass model spring constant k used in Sec. II.

A static mass of the cantilever can be defined as the ratio between k_s and ω_1^2, which for a rectangular beam gives

$$m_s \equiv \frac{k_s}{\omega_1^2} = \frac{k_1/1.030}{\omega_1^2} = \frac{0.25}{1.030} m_c = 0.2425 m_c. \tag{72}$$

The above number coincides with the result given by Sader in Ref. 48.

VI. SUMMARY AND CONCLUSIONS

We have developed a theoretical formalism to describe bimodal AFM experiments. The theory provides different relationships among the bimodal AFM observables and the virial of the interaction and the energy dissipated by the tip-surface forces. The theory is compatible with point-mass and continuous descriptions of the cantilever-tip ensemble. The theory is general. It can be applied to any physical system described by a collection of forced damped oscillators under arbitrary interaction forces.

It is found that the ability of bimodal AFM to provide material contrast depends on the type of representation and on the nonlinear character of the tip-surface force. Parallel-mode representations, where the phase shift (amplitude) of one of the excited modes is plotted vs its own amplitude (phase), do not give material contrast for tip-surface conservative interactions. On the other hand, cross-mode representations, where the phase shift (amplitude) of one of the excited modes is plotted vs the amplitude (phase) of the other, are sensitive to changes in the material properties. The absence of contrast in parallel-mode representations is due to the explicit relationship that exists among dissipation, amplitude, and phase shifts of the same mode. However, in cross-mode representations the relationship is established among the virial and the amplitude of one mode with the phase shift of the other. It is also demonstrated that for linear tip-surface interactions the exact solution of the bimodal AFM system shows the absence of material contrast in both representations.

ACKNOWLEDGMENTS

---

*rgarcia@imm.cnm.csic.es

[1] G. Binnig, C. F. Quate, and C. Gerber, Phys. Rev. Lett. **56**, 930 (1986).

[2] A. Raman, J. Melcher, and R. Tung, Nanotoday **3**, 20 (2008).

[3] Y. Sugimoto, P. Pou, M. Abe, P. Jelinek, R. Perez, S. Morita, and O. Custance, Nature (London) **446**, 64 (2007).

[4] H. Holscher, Appl. Phys. Lett. **89**, 123109 (2006).

[5] A. Engel and D. J. Muller, Nat. Struct. Biol. **7**, 715 (2000).

[6] Y. Seo and W. Jhe, Rep. Prog. Phys. **71**, 016101 (2008).

[7] R. Garcia, R. Magerle, and R. Perez, Nature Mater. **6**, 405 (2007).

[8] Y. J. Li, N. Kobayashi, Y. Naitoh, M. Kageshima, and Y. Sugawara, Appl. Phys. Lett. **92**, 121903 (2008).

[9] M. Ternes, C. P. Lutz, C. F. Hirjibehedin, F. J. Giessibl, and A. J.

Heinrich, Science **319**, 1066 (2008).

[10] A. A. Tseng, A. Notargiacomo, and T. P. Chen, J. Vac. Sci. Technol. B **23**, 877 (2005).

[11] L. Pellegrino, Y. Yanagisawa, M. Ishikawa, T. Matsumoto, H. Tanaka, and T. Kawai, Adv. Mater. (Weinheim, Ger.) **18**, 3099 (2006).

[12] R. V. Martinez, N. S. Losilla, J. Martinez, Y. Huttel, and R. Garcia, Nano Lett. **7**, 1846 (2007).

[13] Y. Martin, C. C. Williams, and H. K. Wickramasinghe, J. Appl. Phys. **61**, 4723 (1987).

[14] S. Crittenden, A. Raman, and R. Reifenberger, Phys. Rev. B **72**, 235422 (2005).

[15] J. Legleiter and T. Kowalewski, Appl. Phys. Lett. **87**, 163120 (2005).

[16] J. Preiner, J. Tang, V. Pastushenko, and P. Hinterdorfer, Phys. Rev. Lett. **99**, 046102 (2007).

[17] S. Kawai, S. Kitamura, D. Kobayashi, S. Meguro, and H. Kawakatsu, Appl. Phys. Lett. **86**, 193107 (2005).

[18] O. Sahin and N. Erina, Nanotechnology **19**, 445717 (2008).

[19] O. Sahin, Phys. Rev. B **77**, 115405 (2008).

[20] O. Sahin, S. Magonov, C. Su, C. F. Quate, and O. Solgaard, Nat. Nanotechnol. **2**, 507 (2007).

[21] O. Sahin, C. F. Quate, O. Solgaard, and A. Atalar, Phys. Rev. B **69**, 165416 (2004).

[22] J. Melcher, S. Hu, and A. Raman, Appl. Phys. Lett. **91**, 053101 (2007).

[23] H. Li, Y. Chen, and L. Dai, Appl. Phys. Lett. **92**, 151903 (2008).

[24] M. K. Ghatkesar, T. Braun, V. Barwich, J. P. Ramseyer, C. Gerber, M. Hegner, and H. P. Lang, Appl. Phys. Lett. **92**, 043106 (2008).

[25] P. Girard, M. Ramonda, and R. Arinero, Rev. Sci. Instrum. **77**, 096105 (2006).

[26] D. W. Dareing, T. Thundat, S. Jeon, and M. Nicholson, J. Appl. Phys. **97**, 084902 (2005).

[27] T. R. Rodriguez and R. Garcia, Appl. Phys. Lett. **84**, 449 (2004).

[28] N. F. Martinez, S. Patil, J. R. Lozano, and R. Garcia, Appl. Phys. Lett. **89**, 153115 (2006).

[29] S. Patil, N. F. Martinez, J. R. Lozano, and R. Garcia, J. Mol. Recognit. **20**, 516 (2007).

[30] N. F. Martinez, J. R. Lozano, E. T. Herruzo, F. Garcia, C. Richter, T. Sulzbach, and R. Garcia, Nanotechnology **19**, 384011 (2008).

[31] D. Platz, E. A. Tholen, D. Pesen, and D. B. Haviland, Appl. Phys. Lett. **92**, 153106 (2008).

[32] S. Jesse, S. V. Kalinin, R. Proksch, A. P. Baddorf, and B. J. Rodriguez, Nanotechnology **18**, 435503 (2007).

[33] R. Proksch, Appl. Phys. Lett. **89**, 113121 (2006).

[34] R. W. Stark, N. Naujoks, and A. Stemmer, Nanotechnology **18**, 065502 (2007).

[35] U. Bostanci, M. K. Abak, O. Aktas, and A. Dana, Appl. Phys. Lett. **92**, 093108 (2008).

[36] A. San Paulo, J. P. Black, R. M. White, and J. Bokor, Appl. Phys. Lett. **91**, 053116 (2007).

[37] B. J. Rodriguez, C. Callahan, S. V. Kalinin, and R. Proksch, Nanotechnology **18**, 475504 (2007).

[38] P. Thota, S. MacLaren, and H. Dankowicz, Appl. Phys. Lett. **91**, 093108 (2007).

[39] C. Dietz, M. Zerson, C. Riesch, A. M. Gigler, R. W. Stark, N. Rehse, and R. Magerle, Appl. Phys. Lett. **92**, 143107 (2008).

[40] J. R. Lozano and R. Garcia, Phys. Rev. Lett. **100**, 076102 (2008).

[41] Á. San Paulo and R. García, Phys. Rev. B **64**, 193411 (2001).

[42] J. B. Marion, *Classical Dynamics of Particles and Systems* (Academic, New York, 1998).

[43] R. Garcia, C. J. Gomez, N. F. Martinez, S. Patil, C. Dietz, and R. Magerle, Phys. Rev. Lett. **97**, 016103 (2006).

[44] R. Garcia and A. San Paulo, Phys. Rev. B **60**, 4961 (1999).

[45] R. W. Stark and W. M. Heckl, Surf. Sci. **457**, 219 (2000).

[46] T. R. Rodriguez and R. Garcia, Appl. Phys. Lett. **80**, 1646 (2002).

[47] H. J. Butt and M. Jaschke, Nanotechnology **6**, 1 (1995).

[48] J. E. Sader, I. Larson, P. Mulvaney, and L. R. White, Rev. Sci. Instrum. **66**, 3789 (1995).